ACS APPLIED ENERGY MATERIALS
Cite This: ACS Appl. Energy Mater. XXXX, XXX, XXX−XXX
Article
www.acsaem.org

Flowerlike Mesoporous $FeF_3{\cdot}0.33H_2O$ with 3D Hierarchical Nanostructure: Size-Controlled Green-Synthesis and Application as Cathodes for Na-Ion Batteries

Min Liu,[†] Lei Liu,[†] Hai Hu,[†] Li Yang,[†] Zhenhua Yang,[†] Ying Wang,*[,‡] and Xianyou Wang*[,†]

[†]National Base for International Science & Technology Cooperation, National Local Joint Engineering Laboratory for Key Materials of New Energy Storage Battery, Hunan Province Key Laboratory of Electrochemical Energy Storage & Conversion, School of Chemistry, Xiangtan University, Xiangtan 411105, China

[‡]Department of Chemistry, University of North Carolina at Chapel Hill, Chapel Hill, North Carolina 27514, United States

Supporting Information

ABSTRACT: A flowerlike mesoporous $FeF_3{\cdot}0.33H_2O$ with three-dimensional (3D) hierarchical nanostructure is successfully prepared for the first time through a facile PEG-assisted solvothermal route. By rationally regulating and controlling the amount of PEG-400 in solvent, a series of nanostructured $FeF_3{\cdot}0.33H_2O$ materials with various morphologies and sizes is obtained. The probable formation mechanism related to the role of the PEG is explored. Furthermore, the electrochemical performances of the as-prepared samples for Na-ion battery (NIB) are investigated and discussed. The flower-like mesoporous $FeF_3{\cdot}0.33H_2O$ can deliver the noticeable initial discharge capacity of 283 mAh g^{-1} and retain 190 mAh g^{-1} after 100 cycles within a potential range of 1.5−4.5 V at 0.1 C. Particularly, even at a high rate of 2.0 C, the material can still exhibit a high capacity of 155 mAh g^{-1}. The excellent electrochemical performances can be attributed to the unique 3D hierarchical porous nanostructure and the small particle size, which can provide large electrode/electrolyte contact area and abundant Na storage sites, facilitate rapid electronic and ionic transportation as well as electrolyte penetration, and accommodate the volume changes of the $FeF_3{\cdot}0.33H_2O$ cathode materials. Therefore, this work provides a facile and scalable strategy to prepare high-performance cathode active materials in the applications of high-capacity NIB.

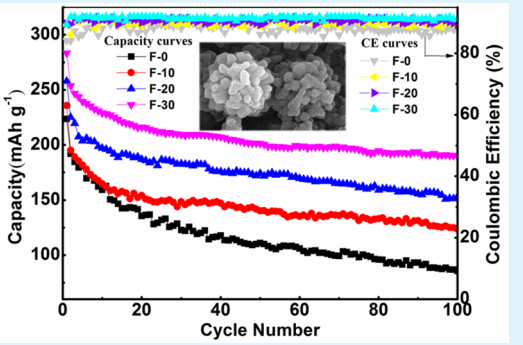

KEYWORDS: *Na-ion batteries, cathode material, iron-based fluoride, 3D hierarchical porous nanostructure, electrochemical performance*

1. INTRODUCTION

A room-temperature Na-ion battery has been considered one of the potential alternatives to a Li-ion battery (LIB) in the grid-scale electrochemical energy storage and conversion due to their cost advantage, resource abundance, as well as their analogous reaction mechanism to LIB based on the extraction/insertion of mobile alkali ions in the structure.[1−5] In recent years, some intercalation-based compounds like layered oxides, polyanions, which are commonly utilized for LIB, have exhibited promising electrochemical properties as cathode active material for NIB.[4−16] Nevertheless, the heavier molar mass as well as the higher standard electrochemical potential of Na (approximately 22.99 g mol^{-1}, −2.71 V) compared to those of Li (approximately 6.94 g mol^{-1}, −3.04 V) usually lead to the lower energy density and operating voltages of NIB, which are not enough to satisfy the high-energy-density requirements.[4] Moreover, ion size of Na (0.102 nm) is 34% larger than that of Li (0.076 nm), which can lead to sluggish ion diffusion kinetics in the electrode structure, thus limiting the practical application of NIB.[1] Hence, in terms of the practical use of NIB, exploring the premium cathodes with much higher energy density and excellent electrochemical performance is crucial to meeting the demand of energy storage devices.

Employing multielectron conversion-type compounds as the cathode material is one of the favorable methods to develop the high-energy NIB systems.[5,17−19] The full utilization of multivalent redox center for conversion cathode materials is beneficial to achieve much higher capacities compared with intercalation-based cathode materials. Among various types of conversion-based compounds, iron-based fluoride has been considered as the most competitive and attractive alternatives for Li/Na-ion batteries because of its high operation voltage, large theoretical specific capacities, inexpensive and low toxicities.[20−29] In particular, $FeF_3{\cdot}0.33H_2O$ with open framework, as one of the polymorph of iron fluorides, possesses unique tunnel structure, which contributes significantly to improving the storage and transportation of sodium.[17,30−34] Nonetheless, the practical development of iron fluorides used

Received: September 18, 2018
Accepted: November 1, 2018
Published: November 1, 2018

DOI: 10.1021/acsaem.8b01585
ACS Appl. Energy Mater. XXXX, XXX, XXX−XXX

Scheme 1. Schematic Illustration for the Preparation Process of $FeF_3{\cdot}0.33H_2O$ Cathode Material with Different Morphologies

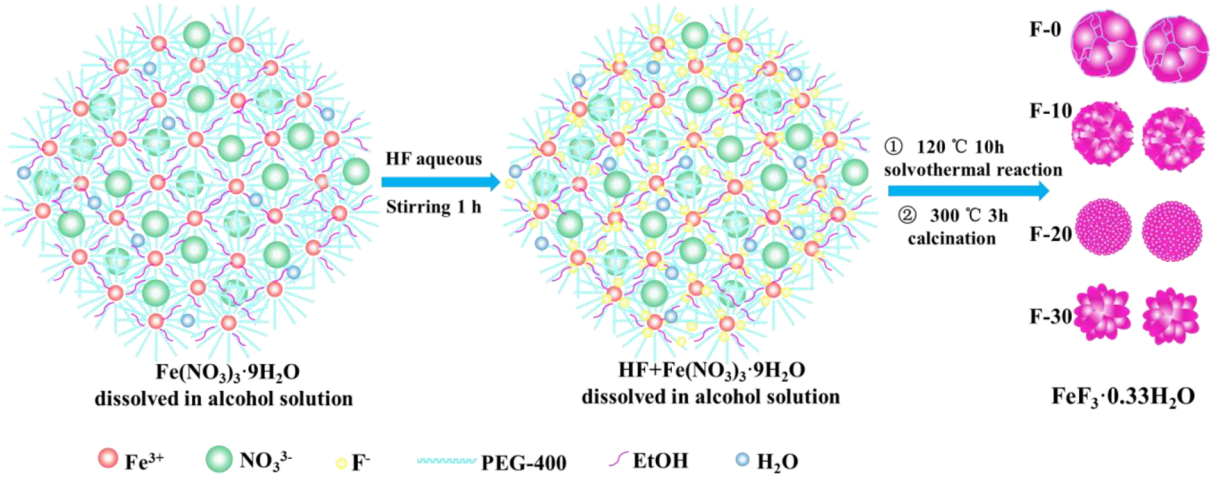

for the cathode materials of NIB has been facing some challenges, e.g., low kinetics and poor electric conductivity arisen from the wide bandgap as well as high ionicity of Fe−F bond.[21,29,35] Furthermore, another obstruction which restricts the practical application of $FeF_3{\cdot}0.33H_2O$ is the large volume variation during the charge/discharge process.[17,36]

In order to overcome above drawbacks, intensive efforts have been focused on doping with other ions (like OH^-, O^{2-}, Ti^{4+}, Cr^{3+}, or Co^{3+}[18,37−42]) to diminish band gap and introducing a conductive additive phase (such as carbon materials, V_2O_5, $AlPO_4$, and MoS_2[20,25,28,31,32,35,43,44]) with iron fluoride to improve electronic conductivity. Although the specific capacity of the iron-based fluoride has been enhanced via the above approaches, it will decrease the energy densities of NIB because the carbon materials as part of the cathode material are not electrochemically active in the batteries.[23,43,44]

Besides, synthesizing nanometer-sized active material is another feasible and effective approach. Rational designing morphologies and controlling size of particles could not only effectively alleviate the volume effect but also shorten the transport pathways of electrons and ions, and nanoscale crystallite dimension could markedly enhance the reaction activity of the $FeF_3{\cdot}0.33H_2O$ particles. Although iron-based fluoride with different nanostructures have been successfully prepared, such as nanospheres,[26,38,45,46] nanowires,[47,48] and hollow microspheres,[46,49] their electrochemical performances still need to be further improved to meet the energy storage requirements. Compared with other nanoscale materials, hierarchical nanostructures via assembling from several nanoparticles possess the larger specific surface area and void, which can provide enough space for alleviating the volume effect as well as electrolyte penetration.[50,51] Recently, some iron-based fluorides with hierarchical nanostructures have been synthesized.[35,49,50] However, their preparation methods are usually complicated as well as high energy consumption, and the raw materials are expensive, which are not conducive to mass production. Moreover, it is not easy to acquire the pure phase $FeF_3{\cdot}0.33H_2O$ due to the uncontrollable side reactions. Apparently, seeking the reasonable and easy strategies to prepare the advanced hierarchical nanoscale iron-based fluoride with homo,geneous and controllable morphology is still a significant challenge.

Polyethylene glycol (average molecular weight 400, abbreviated as PEG-400), a green solvent, possesses a number of benign physical and chemical characteristics, such as nontoxic, low cost, low flammability, biodegradable and nonvolatile. Moreover, PEG-400 is a stable solvent with high boiling point and high viscosity, which has been widely utilized as green reaction media and in the nanostructure formation process as dispersion, solvent, or modifiers.[23,52−56] In view of the current research progress in this field and the mentioned above advantages, here a flowerlike mesoporous $FeF_3{\cdot}0.33H_2O$ with 3D hierarchical nanostructure is successfully synthesized through a facile PEG-assisted solvothermal route. By rationally regulating and controlling the amount of PEG in solvent, restricting the excessive growth rate of the particles and the formation rate of clusters, a series of nanostructured $FeF_3{\cdot}0.33H_2O$ materials with various morphologies and sizes are obtained. The properties of the all as-prepared materials for sodium-ion batteries are systematically characterized by physicochemical and electrochemical tests.

2. EXPERIMENTAL SECTION

2.1. Sample Synthesis. All reagents were utilized without any further purification. A series of controllable nanostructured $FeF_3{\cdot}0.33H_2O$ materials with various sizes and morphologies were fabricated via a facile PEG-assisted solvothermal approach, selecting $Fe(NO_3)_3{\cdot}9H_2O$ (Aldrich) as the iron source, hydrogen fluoride (HF) (40 wt %) as the fluorine source, and the polyethylene glycol (PEG-400) (Aldrich) as the size tuning agent. The preparation process is schematically illustrated in Scheme 1. First, ethanol and PEG-400 in volume ratios of 40:0, 30:10, 20:20, 10:30, and 0:40 were mixed in Teflon-lined autoclave with rigorous stirring for 30 min. The total volume of solvent was kept at 40 mL. Then, 2.02 g $Fe(NO_3)_3{\cdot}9H_2O$ was dissolved into the above five solvents, respectively, and stirred for 30 min. Subsequently, 1 mL of hydrofluoric acid was added dropwise to the above four solutions with stirring for 1 h. Afterward, these mixed solution was then transferred to the Teflon-lined stainless steel autoclaves and heated hermitically at 120 °C for 10 h. Then, centrifugation was performed and the products were washed with ethyl alcohol to remove residual HF and then dried at 80 °C for 12 h. Finally, the collected precursors were further heated at 300 °C in N_2 for 3 h, removing the moisture and organic residues on the surface of materials. The final products synthesized via different volume ratios of PEG and anhydrous ethanol are referred as F-0, F-10, F-20, F-30, and F-40 (Among them, F represents $FeF_3{\cdot}0.33H_2O$ and the Arabic numerals represent the volume of PEG used in the preparation process) for simplicity.

2.2. Material Characterization. Structure, crystallinity, and phase purity of materials were checked from 10° to 80° (2θ) through X-ray diffraction (XRD, Bruker D8) with a Cu Kα radiation.

DOI: 10.1021/acsaem.8b01585
ACS Appl. Energy Mater. XXXX, XXX, XXX−XXX

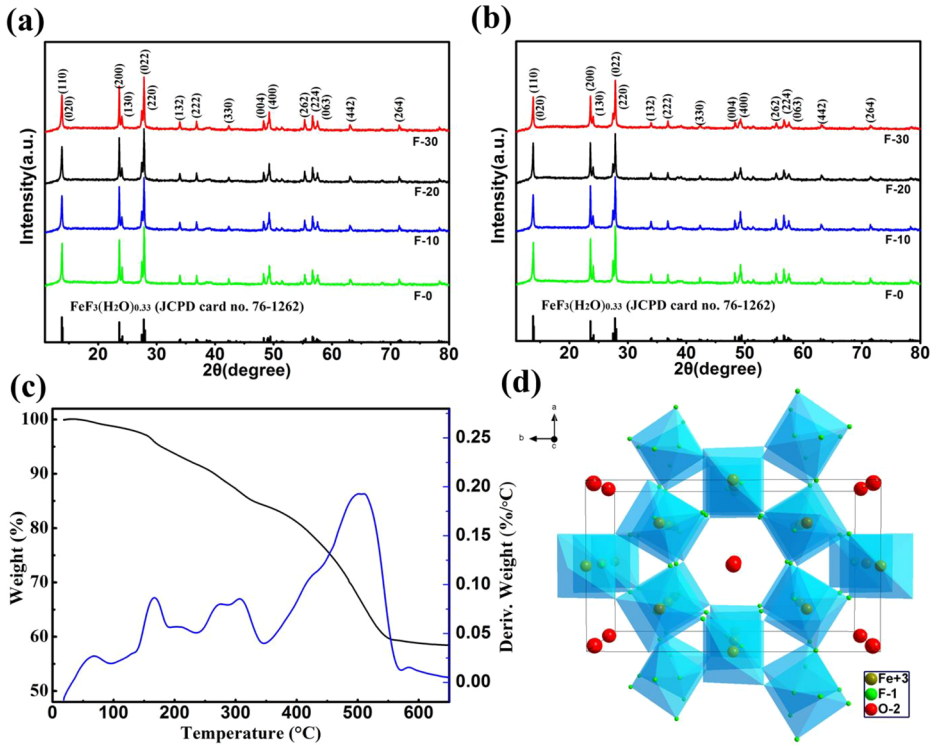

Figure 1. (a) XRD patterns of all final $FeF_3{\cdot}0.33H_2O$ products after calcination at 300 °C for 3 h under N_2, (b) XRD patterns of all $FeF_3{\cdot}0.33H_2O$ precursors before calcinations, (c) thermogravimetric analyses of the as-prepared F-30 precursor, and (d) crystal structure of $FeF_3{\cdot}0.33H_2O$.

Thermogravimetric analysis was undertaken by a Rigaku instrument at the heating speed of 10 °C min^{-1} under N_2. Field-emission scanning electron microscopy (FE-SEM, Quanta FEG250) and transmission electron microscopy (TEM, JEOL JSM-2100F, 200 kV) measurements were carried out to observe the morphology and size of materials. High-resolution microscopy images as well as selected area electron diffraction (SAED) were recorded on a Tecnai G^2 F20 high-resolution transmission electron microscope (HRTEM). N_2 adsorption−desorption isotherms was tested by a Micromeritics TriStar II 3020 analyzer. The N_2 adsorption/desorption isotherms were measured based on the Brunauer−Emmett−Teller (BET) model. The valence state and chemical composition of sample were analyzed by the ESCAlab-250 X-ray photoelectron spectroscopy (XPS).

2.3. Electrochemical Measurement. Electrochemical property of all materials was tested in the coin cells (CR2025-type) using sodium metal as the counter electrode. The working electrodes were synthesized with a slurry of 80% active material, 10% acetylene black (EC), and 10% polyvinylidene fluoride (PVDF) binder. The above mixed materials were dispersed in *N*-methyl-1,2-pyrrolidone (NMP), and the slurry was planted onto aluminum foil. Glass microfiber filters (Whatman) were utilized as the separator. $NaClO_4$ (1 M) in propylene carbonate/ethylene carbonate/diethyl carbonate (PC/EC/DEC, 1:1:1 vol %) was employed as the electrolyte. Generally, the typical mass of active substances was weighed to about 1.5 mg cm^{-2}. The assembly of coin cells was performed in a glovebox with argon gas. The galvanostatic charge/discharge processes of all electrodes were conducted at different rates (1 C = 200 mAh g^{-1}) with a voltage window of 1.5−4.5 V (vs Na^+/Na) on Neware battery test apparatus. Electrochemical impedance spectroscopy (EIS) measurement was conducted via utilizing the VersaSTAT3 Princeton Tester with the amplitudes of 5 mV in a frequency range from 0.01 Hz to 100 kHz.

3. RESULTS AND DISCUSSION

Figure 1a presents the XRD pattern of all final $FeF_3{\cdot}0.33H_2O$ products after calcination at 300 °C in N_2 for 3 h. It can be observed that the final products match well with hexagonal tungsten bronze structure $FeF_3{\cdot}0.33H_2O$ (PDF No. 76-1262), without any impurity signal, showing that the final $FeF_3{\cdot}0.33H_2O$ products were successfully synthesized via the PEG-assisted solvothermal strategy. Compared with XRD patterns of all precursors before calcination (Figure 1b), it can be found that, as the proportion of PEG-400 in the solvent increases, the diffraction peaks of precursors gradually narrowed and weaken, which can be ascribed to its lower crystallinity due to the presence of organic residues and moisture on the surface of particles.[23] Apparently, calcination in N_2 for 3 h is beneficial for obtaining higher crystallinity products. In addition, the calcination temperature of 300 °C is also an ideal temperature by thermogravimetric analyses for the as-prepared F-30 precursor (Figure 1c). Similar to the previous reports, while the temperature is less than 250 °C, the weight loss can be attributed to the removal of the adsorbed water.[23,57] During the temperature region from 250 °C (the boiling point of PEG) to 300 °C, the weight loss is mainly attributed to the evaporation of PEG.[23] The derivative peak at more than 300 °C could be related to the hydration water. As the temperature rises to 330 °C, the hydration water in the material is completely removed, and the weight loss is approximately 5 wt %. When the calcination temperature reaches at 500 °C, the crystal phase of materials is further changed and FeF_3 is partially decomposed to FeF_2.[23] Hence, in order to evaporate PEG without changing the crystal phase of $FeF_3{\cdot}0.33H_2O$, all samples were heated at 300 °C in N_2 for 3 h. After the further calcining, the diffraction peaks of all final $FeF_3{\cdot}0.33H_2O$ products become stronger and sharper than that before calcination, indicating that all final products possess a good crystallinity. Moreover, the cell structure of $FeF_3{\cdot}0.33H_2O$ is shown in Figure 1d where six octahedral FeF_6 is conjoined via the corner-sharing F, resulting in forming the huge hexagonal cavity. The water molecule presented in the $FeF_3{\cdot}0.33H_2O$ tunnel plays a part as the structural stabilizer, which can

DOI: 10.1021/acsaem.8b01585
ACS Appl. Energy Mater. XXXX, XXX, XXX−XXX

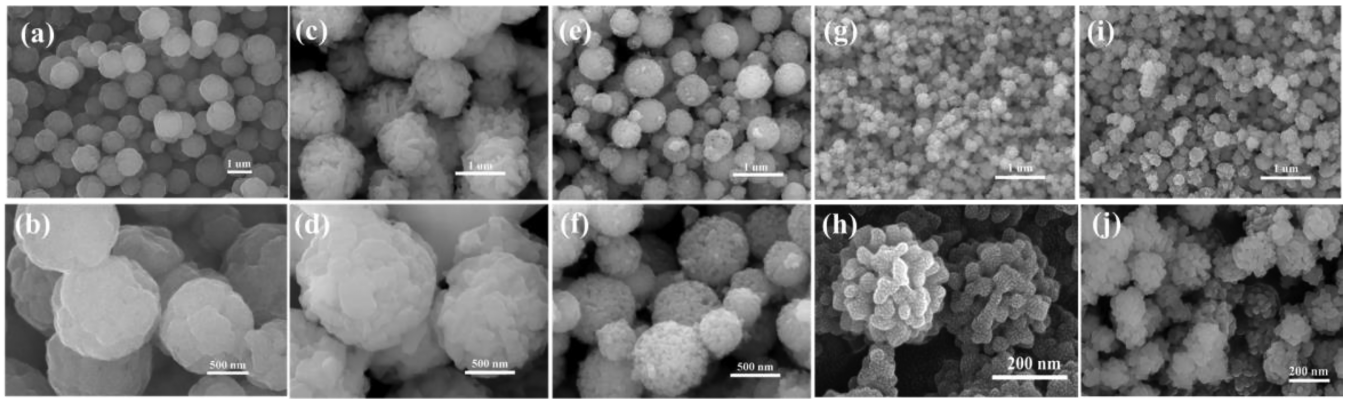

Figure 2. SEM images of (a,b) F-0, (c,d) F-10, (e,f) F-20, (g,h) F-30, and (i,j) F-40.

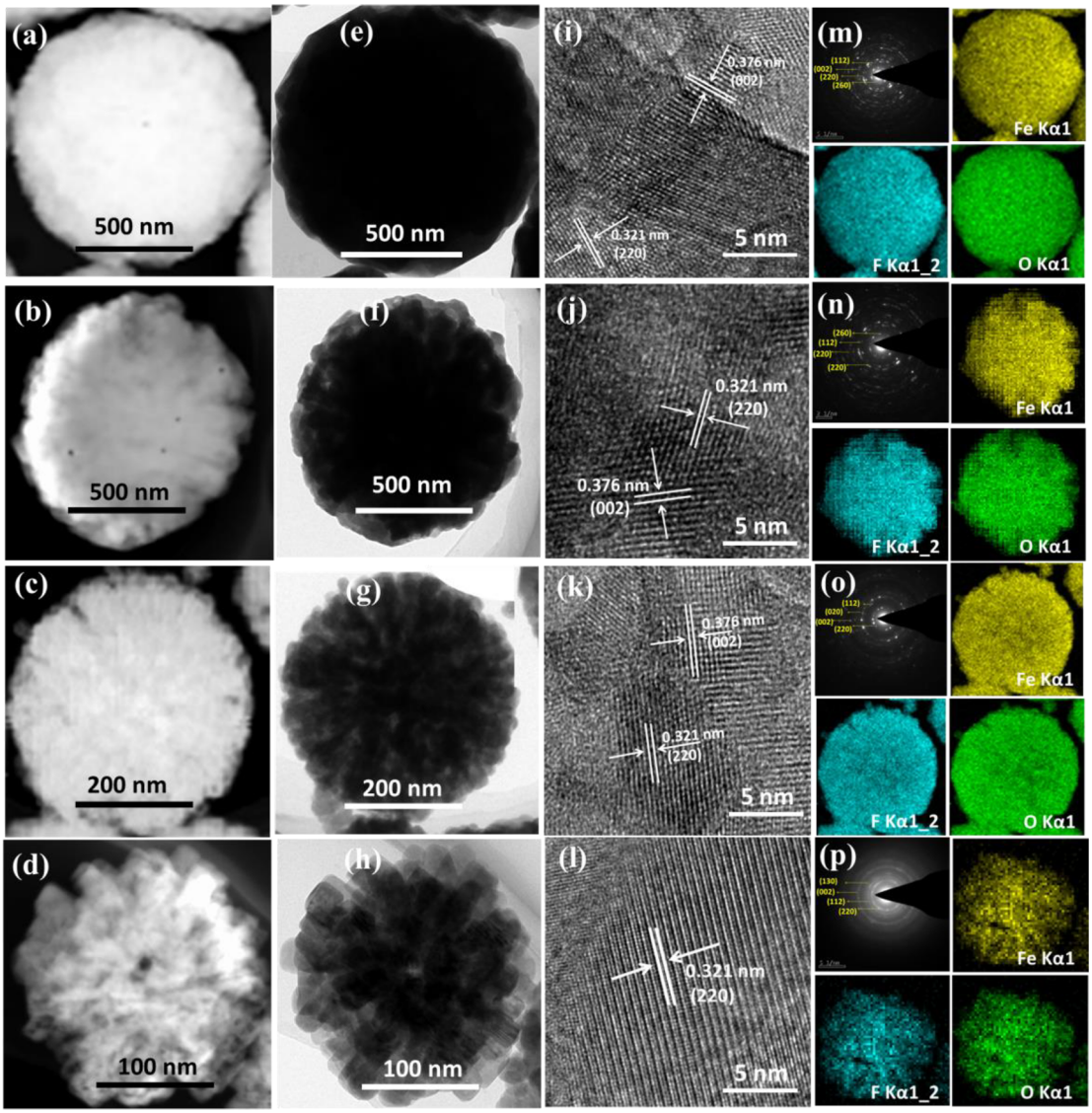

Figure 3. (a) FE-SEM images of (a) F-0, (b) F-10, (c) F-20, and (d) F-30; TEM images of (e) F-0, (f) F-10, (g) F-20, and (h) F-30; HRTEM images of (i) F-0, (j) F-10, (k) F-20, and (l) F-30; SAED patterns and corresponding respective elemental mappings of (m) F-0, (n) F-10, (o) F-20, and (p) F-30.

stabilize the huge hexagonal tunnel and relieve structure collapse upon cycling.[17,24,35] Thus, the open structure of $FeF_3 \cdot 0.33H_2O$ is beneficial for accommodation and transport of Na^+ ions.

The changes of particle size and morphology of the final $FeF_3 \cdot 0.33H_2O$ samples are analyzed by SEM. As being observed from Figure 2, the particle size and morphology of the as-prepared materials change slightly with the varying of

DOI: 10.1021/acsaem.8b01585
ACS Appl. Energy Mater. XXXX, XXX, XXX−XXX

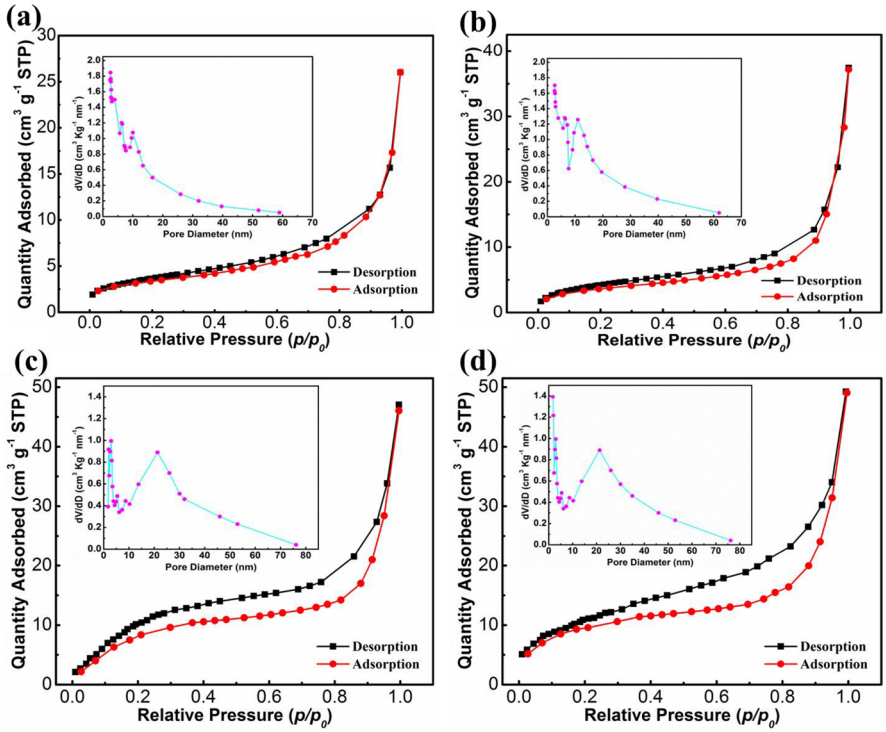

Figure 4. (a) Nitrogen adsorption/desorption isotherms of (a) F-0, (b) F-10, (c) F-20, and (d) F-30; inset, BJH pore size distribution plots.

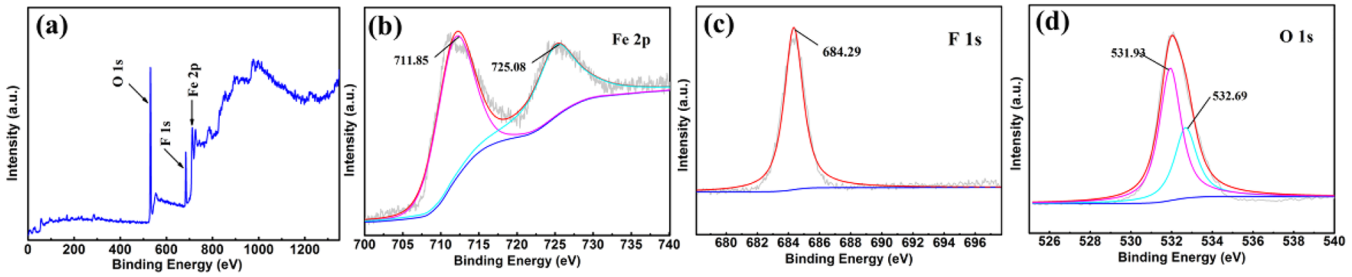

Figure 5. XPS spectra of (a) survey spectrum, (b) Fe 2p region, (c) F 1s region, and (d) O 1s region for F-30 cathode.

the ratio of PEG-400 in the solvent. The pristine $FeF_3 \cdot 0.33H_2O$ (F-0, Figure 2a,b) presents approximately 1 μm uniform microspheres with relatively smooth surfaces. With the increase of the amount of PEG-400 from 10 to 30 mL, the morphologies of the samples show a successive change from rough microspheres with about 1 μm diameter (F-10, Figure 2c,d) to inhomogeneous spheres with micronanostructure (F-20, Figure 2e,f) and finally transform into homogeneous flowerlike nanostructure (~200 nm) with 3D hierarchical mesoporous structure (F-30, Figure 2g,h). However, when the amount of PEG-400 is further raised to 40 mL, the particle size dose not decrease further and the particles become inhomogeneous and agglomerate (F-40, Figure 2i,j). The above phenomena indicate that the morphology of $FeF_3 \cdot 0.33H_2O$ prepared through a PEG-assisted solvothermal method is controllable by tuning the amount of PEG-400 in the reaction system.

The details of the changes in the morphology and grain size of the prepared samples are further investigated by FE-SEM and TEM images. As displayed in Figure 3a,e, F-0 displays a regular microspherical structure with approximately 1 μm diameter. From Figure 3b,f, it can be seen that the edges of F-10 nanospheres appear irregular. In Figure 3c,g, F-20 is constructed with dozens of homogeneous nanoparticles and possesses a hierarchical porous spherical structure. As illustrated in Figure 3d,h, F-30 is self-assembled from some nanorods with a thickness of about 20 nm. They are connected to each other through the center of the particles and exhibit a flowerlike shape with a layered mesoporous structure. Through analysis of the HRTEM images (Figure 3i–l), the lattice fringe marked by white arrow is measured to be 0.32 nm, which corresponds to (220) plane of $FeF_3 \cdot 0.33H_2O$. In addition, the corresponding SAED analysis (the upper left of Figure 3m–p) verifies the products belong to $FeF_3 \cdot 0.33H_2O$. Moreover, the elemental mappings confirm that the Fe, F, and O elements are evenly distributed throughout the grains, thus inferring that the elements coprecipitated in each particle, rather than progressively separated in different particles.

To demonstrate the hierarchical mesoporous structure and pore-size distribution of all samples, the BET technique was employed. The nitrogen adsorption/desorption isotherms as well as the corresponding pore diameter distribution curves (inset) of F-0, F-10, F-20, and F-30 are displayed in Figure 4a–d, respectively. As being seen from figures, all samples possess the similar type of isotherm, i.e., type IV, suggesting the presence of mesoporous structure. The BET surface areas of F-

DOI: 10.1021/acsaem.8b01585
ACS Appl. Energy Mater. XXXX, XXX, XXX–XXX

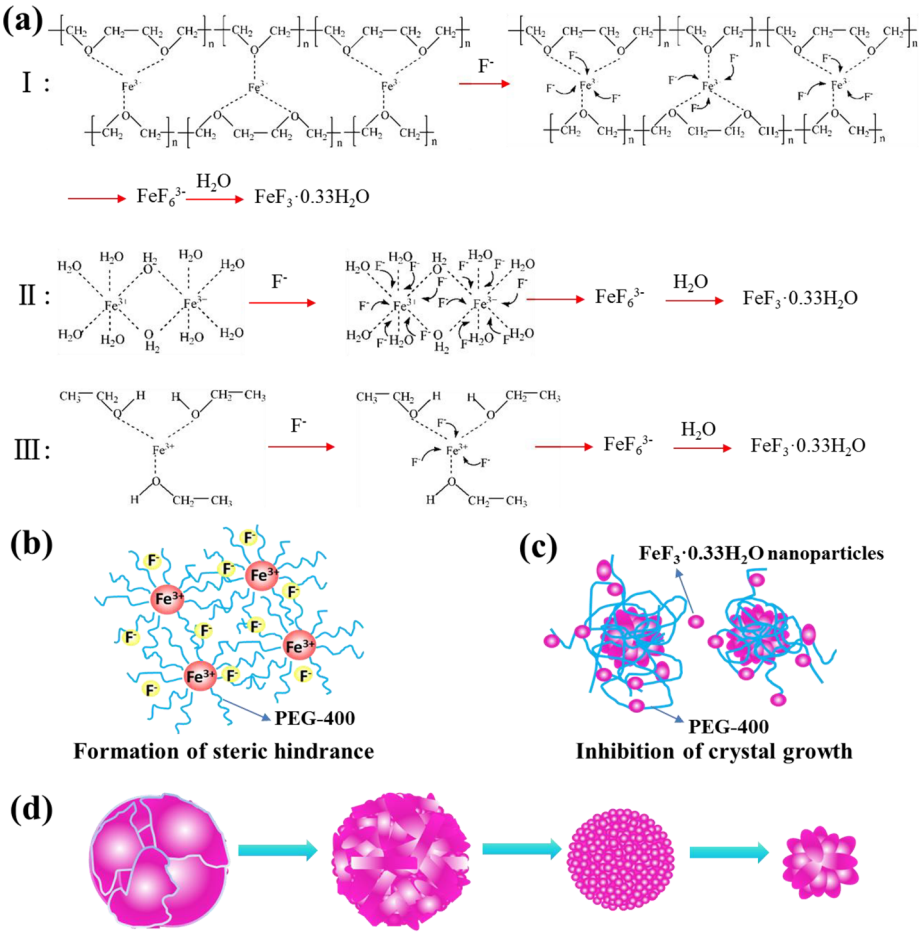

Figure 6. (a) Schematic diagram for three chemical reaction routes in solution. Schematic diagram of the effect of PEG-400 on (b) the chemical reaction and (c) the crystal formation. (d) Schematic diagram of the morphology evolution of $FeF_3{\cdot}0.33H_2O$ with the increase of the amount of PEG-400.

0, F-10, and F-20 are calculated to be approximately 12.8, 16.5, and 20.6 $m^2\ g^{-1}$, respectively. While F-30 sample presents the largest specific surface area of 25.8 $m^2\ g^{-1}$. Correspondingly, pore diameter distribution of F-0, F-10, F-20, and F-30 was 10.24, 11.98, 19.85, and 21.05 nm, respectively. In general, appropriate porous structure as well as specific surface area cannot only facilitate the transportation of Na^+ but also increase the contact region between the cathode and electrolyte, thus further enhancing the electrochemical performances of iron fluoride cathode material. Furthermore, the hierarchical porous structure can efficiently accommodate the volume changes of the cathode material during charge/discharge process, thus maintaining the structural integrity of iron fluoride and resulting in a better cycle stability.[23,49,50] Apparently, compared with other three samples, the F-30 sample with the largest specific surface area and characteristic hierarchical mesoporous structure can facilitate electrolyte accessibility and rapid Na^+ diffusion.

To further characterize the chemical composition and valence state of F-30 cathode, XPS spectra were recorded. The survey XPS spectrum of F-30 depicted in Figure 5a revealed the existence of Fe, F, and O elements in the material. As displayed in Figure 5b, the XPS spectra of Fe 2p show two main peaks located at 711.85 and 725.08 eV, which correspond to Fe $2p_{3/2}$ and Fe $2p_{1/2}$ of the bond energy of Fe^{3+}−F.[35,37] As observed the F 1s region in Figure 5c, one main peak centered at about 684.29 eV is assigned to F−Fe bonding. As presented in Figure 5d, it is found that the peak of O 1s exhibits the two spectra. In one aspect, the board peak at approximately 531.93 eV corresponding to the O−H bond may derive from the H_2O molecules in the huge hexagonal tunnel. In another aspect, a weak peak at approximately 532.69 eV is related to the bond energy of O−H from the hydration H_2O participated in the formation of the crystalline structure.[35]

As we all know, the polyethylene glycol, as a nonionic surfactant, possesses hydrophobic $-CH_2-CH_2-$ and hydrophilic −O− radicals on the chains. It follows that PEG-400 can be well dissolved in water in any ratio and a great deal of oxygen atoms on PEG chains will easily combine with metal ions such as Zn^{2+}, Al^{3+}, Fe^{3+} to form the flocculated agglomerates or cross-linked system.[23,52,58,59] As shown in route (I) of Figure 6a, the solvated Fe^{3+} combine with oxygen atoms on PEG chains to form the flocculated agglomerates. Once high electronegativity F^- were added in the solution, they will replace oxygen atoms from different spatial locations to form FeF_6^{3-}, which in turn generates $FeF_3{\cdot}0.33H_2O$ nanoparticles.[57,60] Compared with routes (II) and (III), PEG-400 has a more pronounced effect on chemical reaction process. On the one hand, during the nucleation process, PEG induces the formation of rod-shaped fluoride by the structure-directing action of its terminal hydroxyl group. Then, the rod-shaped nanoparticles are self-assembled into various morphological samples. On the other hand, the large viscosity, low fluidity, and high molecular weight of PEG will affect the

DOI: 10.1021/acsaem.8b01585
ACS Appl. Energy Mater. XXXX, XXX, XXX−XXX

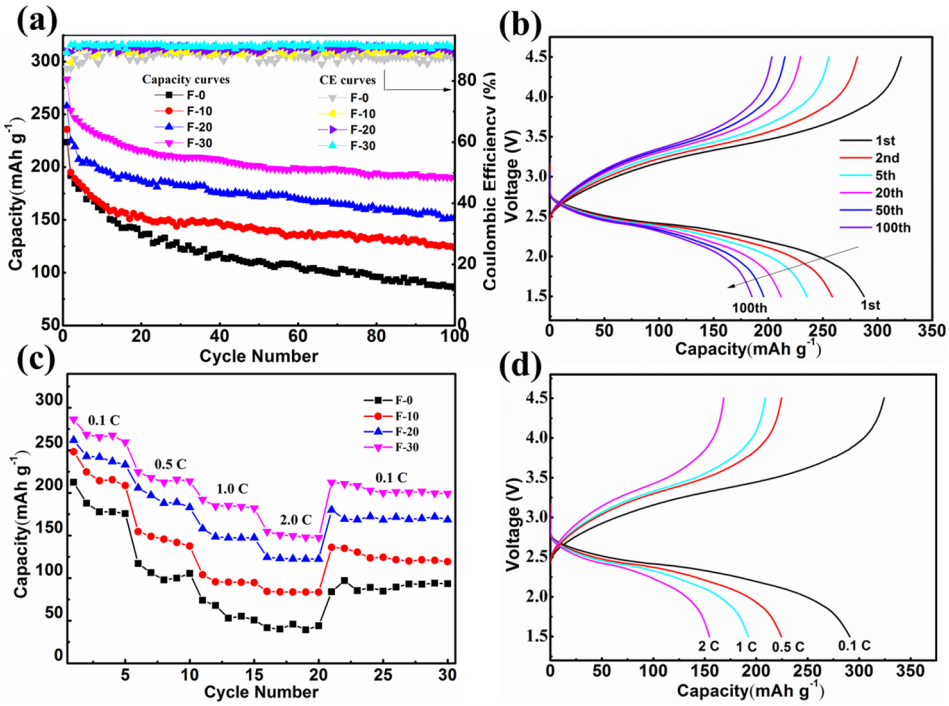

Figure 7. (a) Cycling performances of all the electrodes at 0.1 C within the voltage range of 1.5−4.5 V. (b) Charge−discharge curves of F-30 electrode at 0.1 C. (c) Rate capabilities of all the electrodes varying rates from 0.1 to 2 C. (d) The initial discharge and charge profiles of F-30 electrode in the current density range of 0.1−2 C.

Table 1. Comparisons of the Electrochemical Performances for Different Morphology Iron Fluorides as Cathode Material of NIB

sample no.	morphology	voltage window/V	current density/ mA g^{-1}	cycle performance	ref
1	flowerlike mesoporous $FeF_3{\cdot}0.33H_2O$ with 3D hierarchical nanostructure (~200 nm)	1.5−4.5	20	190 mAh g^{-1} after 100 cycles	this work
2	hollow porous $FeF_3{\cdot}0.33H_2O$ microspheres(~1 μm)	1.2−4.0	20	117 mAh g^{-1} after 80 cycles	35
3	particle with irregular morphology (diameter distribution with 5−7 μm)	1.0−4.0	237	105 mAh g^{-1} after 40 cycles	32
4	particle with microstructured shape aggregated from nanoparticles (~10 nm)	1.2−4.0	23.7	74 mAh g^{-1} after 50 cycles	30

reaction kinetics, further affecting the growth and crystallization processes of $FeF_3{\cdot}0.33H_2O$.[52,54,61] When no PEG-400 is added, the barriers deriving from the surfactant electrostatic interactions and steric hindrance of PEG-400 are absent and the particles grow large as well as homogeneous in morphology (as F-0 shown in Figure 2a,b). Nevertheless, as shown in Figure 6b,c, after adding PEG-400, steric hindrance formed due to their large viscosity and the long chains, which constrained the nucleation and growth of $FeF_3{\cdot}0.33H_2O$, leading to inhomogeneous morphologies and reduced sizes, as F-10 and F-20 demonstrated in Figure 2. As the amount of PEG-400 increased, particle size gradually shrinks, while the surface of particle is also getting rougher (Figure 6d). Obviously, a small quantity of PEG-400 (10 and 20 mL) is not sufficient to completely limit the nucleation and growth of $FeF_3{\cdot}0.33H_2O$. When the amount of PEG-400 is increased to a certain volume (30 mL), which can be enough to significantly restrict the growth crystallization of the iron fluorides. Thereby a uniform flowerlike mesoporous $FeF_3{\cdot}0.33H_2O$ with 3D hierarchical nanostructure can be obtained. Nevertheless, while the volume of PEG-400 further increased to 40 mL (Figure 2i,j), nanoparticles with inhomogeneous morphologies are observed due to the effect of encapsulating and attaching particles of PEG-400, making the particles aggregate to form a linear cluster and the cluster size grow larger.[52,61] This phenomenon confirmed that PEG-400 plays a vital role in the nucleation, growth, as well as crystallization evolutions of $FeF_3{\cdot}0.33H_2O$. Of course, the more elaborate formation mechanism for the morphology change with the auxiliary of PEG-400 needs to be further researched in the next study.

The cycling performances of $FeF_3{\cdot}0.33H_2O$ with different morphology were characterized at 0.1 C in the 1.5−4.5 V range, as presented in Figure 7a. F-0, F-10, F-20, and F-30 electrodes deliver initial discharge specific capacities of 213, 236, 258, and 283 mAh g^{-1}, respectively. It is worth noting that the specific capacities of all samples in the first cycle show a large and rapid attenuation, which could be associated with the irreversible formation of solid electrolyte interphase (SEI) in the first cycle.[38] With the increase of cycle number, the specific capacity of F-0 shows a fast decay and possesses only 86 mAh g^{-1}, with the retention rate of 30.9% of its initial value after 100 cycles. By contrast, the discharge specific capacity of F-10, F-20, and F-30 are 124, 153, and 190 mAh g^{-1} after 100 cycles, respectively. Furthermore, the Coulombic efficiency (CEs) of

DOI: 10.1021/acsaem.8b01585
ACS Appl. Energy Mater. XXXX, XXX, XXX−XXX

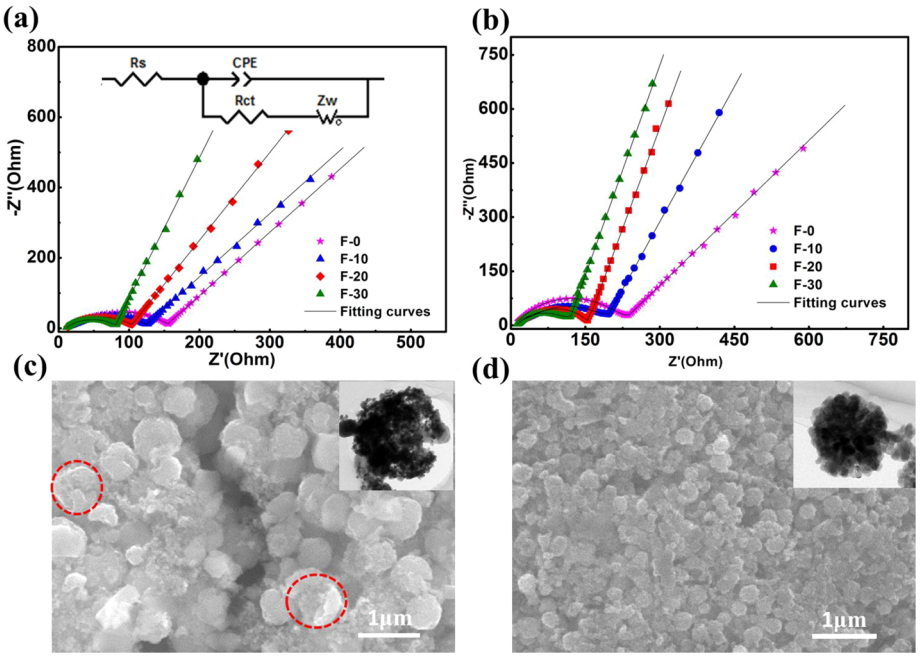

Figure 8. Nyquist plots of all the electrodes after (a) 50 and (b) 100 cycles at 0.1 C, respectively; inset in part a is the equivalent circuit model. SEM images of (c) F-0 and (d) F-30 after 100 cycles; insets, TEM images of corresponding electrodes.

F-30 is generally maintained above 90%, suggesting it has a perfect reversibility and excellent cycle stability. Notably, as shown in Table 1, the cycling performance of F-30 is superior to those of other morphology $FeF_3{\cdot}0.33H_2O$ as cathode materials of NIB according to previous reports.[30,32,35]

To further investigate the electrochemical performance of all samples, the charge/discharge curves at different cycles were presented in Figure 7b and Figure S1a−c. As being observed, all samples show one voltage platform in the initial discharge curve of approximately 2.5 V, which can be attributed to the sodium ion insertion to the HTB $FeF_3{\cdot}0.33H_2O$ framework, whereas the voltage plateau gradually shift to lower voltage with the increase of cycle numbers, which suggests that electrochemical polarization of electrodes become more and more serious. Among the four charge/discharge profiles, the F-30 electrode (Figure 7b) presents the highest discharge voltage plateau as well as the lowest charge voltage plateau, which indicates that it possesses the smallest electrochemical polarization. Apparently, the cycle performance of F-30 was significantly improved and better than three other kinds of cathodes, thus F-30 sample displays a favorable structural reversibility and eminent cycling stability, which benefit from their appropriate particle size and particular hierarchical mesoporous structure.

The rate capabilities of all samples at different rates were also characterized and shown in Figure 7c. The corresponding initial charge/discharge curves for all electrodes at different rates between 1.5 and 4.5 V are shown in Figure 7d and Figure S2a−c. When the rate increases from 0.1 to 2.0 C, the rate capacities of all the electrodes show a trend of decreasing gradient, which may be caused by the slightly increased polarization. The initial discharge capacity of F-0, F-10, and F-20 are 42, 85, and 125 mAh g^{-1} at 2.0 C, respectively. However, among all the electrodes, the capacity loss of F-30 is minimal with the increase current density. The F-30 electrode displays the outstanding rate performance with capacities of 285, 225, 192, and 155 mAh g^{-1} at the rate of 0.1, 0.5, 1.0, and 2.0 C, respectively, and no acute polarization degradation is seen. When the current densities return to 0.1 C after 30 cycles, F-0, F-10, F-20, and F-30 samples can retain a reversible capacity of 84, 136, 180, and 221 mAh g^{-1} with retentions of 39.4%, 54.8%, 68.7%, and 77.5%, respectively, which further show that the F-30 sample presents favorable cycle property and remarkable rate capacity. Such excellent performance of F-30 can be attributed to the unique hierarchical structure as well as the tiny nanoparticle.

To further research electrochemical kinetics of samples, the EIS measurement was conducted. The EIS profiles of all cathodes operated after 50 and 100 cycles at 0.1 C are presented in Figure 8a,b, respectively. The EIS patterns of four electrodes possess similar features and show a semicircle in high-frequency region and a slope in low-frequency region. The semicircle is related to the charge transfer resistance (R_{ct}), and the slope corresponds to the Warburg impedance (Z_w) of sodium ion diffusion into the cathode. Besides, the R_s represents electrolyte resistance, and an equivalent circuit is displayed in the inset of Figure 8a. As shown in Figure 8a, the values of R_{ct} for the F-0, F-10, F-20, and F-30 after 50 cycles are 155.6, 126.4, 104.7, and 81.9 Ω, respectively. After 100 cycles (Figure 8b), the values of R_{ct} for the F-0, F-10, and F-20 samples increase to 236.9, 197.8, and 154.5 Ω with an increment of 81.3, 71.3, and 49.8 Ω. In a sharp contrast, the value of R_{ct} for F-30 sample only increases to 116.8 Ω with an increment of 34.9 Ω. The F-30 possesses the smallest increment of R_{ct} value, indicating that it has the smallest electrochemical polarization. It is probably related to the appropriate shape and unique hierarchical porous structure characteristic of F-30, which shorten the transport pathway of Na^+ and facilitate the penetration of electrolyte, and thus lead to perfect rate capability and cycle capacity.[49,62,63]

In order to further investigate morphological changes during the cycling process, SEM and TEM (inset) analyses of F-0 and F-30 electrodes were conducted after 100 cycles. As being seen in Figure 8c, the spherical structure of the F-0 sample marked

DOI: 10.1021/acsaem.8b01585
ACS Appl. Energy Mater. XXXX, XXX, XXX−XXX

with a red cycle is damaged during the charging/discharging process. However, the flowerlike hierarchical nanostructure of F-30 did not display any significant structural change after 100 cycles (Figure 8d). Such studies revealed excellent mechanical integrity of the F-30 electrode after cycling, which maintained its flowerlike hierarchical nanostructure. Consequently, the remarkable electrochemical performance of F-30 can be ascribed to the appropriate nanometer size and regular morphology, maintaining the efficient contact areas between the electrolyte and cathode material as well as homogeneous intercalation reversibility for Na^+ during cycling. Simultaneously, the micromatrix assembled from nanoscale primary particles not only consolidates the integrity of the host structure but also shortens the transfer pathway of Na^+. Accordingly, the abundant pore structure, on the one hand, facilitates the penetration of electrolyte; on the other hand, it can accommodate the volume changes during repeated Na^+ insertion/extraction processes, thus enhancing the rate capacity and keeping the structural stability of the iron fluorides.

4. CONCLUSIONS

A flowerlike mesoporous $FeF_3{\cdot}0.33H_2O$ was prepared through a facile and low-cost PEG-assisted solvothermal route. This green-synthesis route is not only environmentally-friendly, but also the morphology and size of iron-based fluoride can be easily controlled by tuning the volume ratio of PEG in the mixed solvent. Moreover, PEG-400 plays a crucial role in restricting the excessive growth of the particles and the formation of the cluster. The flowerlike mesoporous $FeF_3{\cdot}0.33H_2O$ (F-30) with 3D hierarchical nanostructure exhibited optimal electrochemical properties among all materials, as the cathode material of NIB it can deliver a high initial capacity of 283 mAh g^{-1} with the residual capacity of 190 mAh g^{-1} after 100 cycles and excellent rate capability and cycle stability. The enhanced electrochemical performances can be mainly attributed to the appropriate particle size and the unique 3D hierarchical porous nanostructure, which are in favor of improving structure stability of the $FeF_3{\cdot}0.33H_2O$ cathode material and shortening the diffusion pathway of Na^+. Therefore, the facile green-synthesis of iron-based fluorides with controllable size and morphology may offer a promising avenue for the fabrication of advanced cathode materials of NIB with excellent performances.

■ ASSOCIATED CONTENT

Supporting Information

The Supporting Information is available free of charge on the ACS Publications website at DOI: 10.1021/acsaem.8b01585.

Electrochemical properties of the F-0, F-10, and F-20 electrodes (PDF)

■ AUTHOR INFORMATION

Corresponding Authors

*Phone: +1 984-234-8489. E-mail: beth.ying.wang@gmail.com.

*Phone: +86 731 58293377. E-mail: wxianyou@yahoo.com.

ORCID

Xianyou Wang: 0000-0001-8888-6405

Notes

The authors declare no competing financial interest.

■ ACKNOWLEDGMENTS

This work is supported financially by the National Natural Science Foundation of China under Project No. 51272221 and the Key Project of Strategic New Industry of Hunan Province under Project Nos. 2016GK4005 and 2016GK4030.

■ REFERENCES

(1) Slater, M. D.; Kim, D.; Lee, E.; Johnson, C. S. Sodium-Ion Batteries. *Adv. Funct. Mater.* **2013**, *23* (8), 947−958.

(2) Hwang, J.-Y.; Myung, S.-T.; Sun, Y.-K. Sodium-Ion Batteries: Present and Future. *Chem. Soc. Rev.* **2017**, *46* (12), 3529−3614.

(3) Kim, H.; Kim, H.; Ding, Z.; Lee, M. H.; Lim, K.; Yoon, G.; Kang, K. Recent Progress in Electrode Materials for Sodium-Ion Batteries. *Adv. Energy Mater.* **2016**, *6* (19), 1600943.

(4) Xiang, X.; Zhang, K.; Chen, J. Recent Advances and Prospects of Cathode Materials for Sodium-Ion Batteries. *Adv. Mater.* **2015**, *27* (36), 5343−5364.

(5) Fang, C.; Huang, Y.; Zhang, W.; Han, J.; Deng, Z.; Cao, Y.; Yang, H. Routes to High Energy Cathodes of Sodium-Ion Batteries. *Adv. Energy Mater.* **2016**, *6* (5), 1501727.

(6) Kim, S.-W.; Seo, D.-H.; Ma, X.; Ceder, G.; Kang, K. Electrode Materials for Rechargeable Sodium-Ion Batteries: Potential Alternatives to Current Lithium-Ion Batteries. *Adv. Energy Mater.* **2012**, *2* (7), 710−721.

(7) Han, M. H.; Gonzalo, E.; Singh, G.; Rojo, T. A Comprehensive Review of Sodium Layered Oxides: Powerful Cathodes for Na-Ion Batteries. *Energy Environ. Sci.* **2015**, *8* (1), 81−102.

(8) Kundu, D.; Talaie, E.; Duffort, V.; Nazar, L. F. The Emerging Chemistry of Sodium Ion Batteries for Electrochemical Energy Storage. *Angew. Chem., Int. Ed.* **2015**, *54* (11), 3431−3448.

(9) Dong, Y.; Li, S.; Zhao, K.; Han, C.; Chen, W.; Wang, B.; Wang, L.; Xu, B.; Wei, Q.; Zhang, L.; Xu, X.; Mai, L. Hierarchical Zigzag $Na_{1.25}V_3O_8$ Nanowires with Topotactically Encoded Superior Performance for Sodium-Ion Battery Cathodes. *Energy Environ. Sci.* **2015**, *8* (4), 1267−1275.

(10) Xu, Y.; Wei, Q.; Xu, C.; Li, Q.; An, Q.; Zhang, P.; Sheng, J.; Zhou, L.; Mai, L. Layer-by-Layer $Na_3V_2(PO_4)_3$ Embedded in Reduced Graphene Oxide as Superior Rate and Ultralong-Life Sodium-Ion Battery Cathode. *Adv. Energy Mater.* **2016**, *6* (14), 1600389.

(11) Gocheva, I. D.; Nishijima, M.; Doi, T.; Okada, S.; Yamaki, J.; Nishida, T. Mechanochemical Synthesis of $NaMF_3$ (M = Fe, Mn, Ni) and Their Electrochemical Properties as Positive Electrode Materials for Sodium Batteries. *J. Power Sources* **2009**, *187* (1), 247−252.

(12) Liang, J.; Wei, Z.; Wang, C.; Ma, J. Vacancy-Induced Sodium-Ion Storage in N-Doped Carbon Nanofiber@MoS_2 Nanosheet Arrays. *Electrochim. Acta* **2018**, *285*, 301−308.

(13) Huang, J.; Wei, Z.; Liao, J.; Ni, W.; Wang, C.; Ma, J. Molybdenum and Tungsten Chalcogenides for Lithium/Sodium-Ion Batteries: Beyond MoS_2. *J. Energy Chem.* **2018**, *9*, 1−25.

(14) Fan, L.; Li, X. Recent Advances in Effective Protection of Sodium Metal Anode. *Nano Energy* **2018**, *53*, 630−642.

(15) Song, X.; Li, X.; Bai, Z.; Yan, B.; Xiong, D.; Lin, L.; Zhao, H.; Li, D.; Shao, Y. Rationally-Designed Configuration of Directly-Coated Ni_3S_2/Ni Electrode by RGO Providing Superior Sodium Storage. *Carbon* **2018**, *133*, 14−22.

(16) Wei, Z.; Wang, L.; Zhuo, M.; Ni, W.; Wang, H.; Ma, J. Layered Tin Sulfide and Selenide Anode Materials for Li- and Na-ion Batteries. *J. Mater. Chem. A* **2018**, *6*, 12185−12214.

(17) Kim, J.; Kim, H.; Kang, K. Conversion-Based Cathode Materials for Rechargeable Sodium Batteries. *Adv. Energy Mater.* **2018**, *8* (17), 1702646.

(18) Zhou, Y.-N.; Sina, M.; Pereira, N.; Yu, X.; Amatucci, G. G.; Yang, X.-Q.; Cosandey, F.; Nam, K.-W. $FeO_{0.7}F_{1.3}$/C Nanocomposite as a High-Capacity Cathode Material for Sodium-Ion Batteries. *Adv. Funct. Mater.* **2015**, *25* (5), 696−703.

DOI: 10.1021/acsaem.8b01585
ACS Appl. Energy Mater. XXXX, XXX, XXX−XXX

(19) Xiao, Y.; Lee, S. H.; Sun, Y.-K. The Application of Metal Sulfides in Sodium Ion Batteries. *Adv. Energy Mater.* **2017**, *7* (3), 1601329.
(20) Shen, Y.; Wang, X.; Hu, H.; Jiang, M.; Yang, X.; Shu, H. A Graphene Loading Heterogeneous Hydrated Forms Iron Based Fluoride Nanocomposite as Novel and High-Capacity Cathode Material for Lithium/Sodium Ion Batteries. *J. Power Sources* **2015**, *283*, 204−210.
(21) Badway, F.; Pereira, N.; Cosandey, F.; Amatucci, G. G. Carbon-Metal Fluoride Nanocomposites. *J. Electrochem. Soc.* **2003**, *150* (9), A1209.
(22) Arai, H.; Okada, S.; Sakurai, Y.; Yamaki, J. Cathode Performance and Voltage Estimation of Metal Trihalides. *J. Power Sources* **1997**, *68* (2), 716−719.
(23) Bai, Y.; Zhou, X.; Zhan, C.; Ma, L.; Yuan, Y.; Wu, C.; Chen, M.; Chen, G.; Ni, Q.; Wu, F.; Shahbazian-Yassar, R.; Wu, T.; Lu, J.; Amine, K. 3D Hierarchical Nano-Flake/Micro-Flower Iron Fluoride with Hydration Water Induced Tunnels for Secondary Lithium Battery Cathodes. *Nano Energy* **2017**, *32*, 10−18.
(24) Cao, D.; Yin, C.; Zhang, J.; Li, C. Bronze and Pyrochlore Type Iron Fluorides as Cathode Materials for Li/Na Batteries. *Kexue Tongbao* **2017**, *62* (9), 897−907.
(25) Ali, G.; Oh, S. H.; Kim, S. Y.; Kim, J. Y.; Cho, B. W.; Chung, K. Y. An Open-Framework Iron Fluoride and Reduced Graphene Oxide Nanocomposite as a High-Capacity Cathode Material for Na-Ion Batteries. *J. Mater. Chem. A* **2015**, *3* (19), 10258−10266.
(26) Chu, Q.; Xing, Z.; Tian, J.; Ren, X.; Asiri, A. M.; Al-Youbi, A. O.; Alamry, K. A.; Sun, X. Facile Preparation of Porous FeF_3 Nanospheres as Cathode Materials for Rechargeable Lithium-Ion Batteries. *J. Power Sources* **2013**, *236*, 188−191.
(27) Li, C.; Yin, C.; Gu, L.; Dinnebier, R. E.; Mu, X.; van Aken, P. A.; Maier, J. An $FeF_3{\cdot}0.5H_2O$ Polytype: A Microporous Framework Compound with Intersecting Tunnels for Li and Na Batteries. *J. Am. Chem. Soc.* **2013**, *135* (31), 11425−11428.
(28) Li, C.; Gu, L.; Tong, J.; Maier, J. Carbon Nanotube Wiring of Electrodes for High-Rate Lithium Batteries Using an Imidazolium-Based Ionic Liquid Precursor as Dispersant and Binder: A Case Study on Iron Fluoride Nanoparticles. *ACS Nano* **2011**, *5* (4), 2930−2938.
(29) Li, C.; Gu, L.; Tsukimoto, S.; van Aken, P. A.; Maier, J. Low-Temperature Ionic-Liquid-Based Synthesis of Nanostructured Iron-Based Fluoride Cathodes for Lithium Batteries. *Adv. Mater.* **2010**, *22* (33), 3650−3654.
(30) Li, C.; Yin, C.; Mu, X.; Maier, J. Top-Down Synthesis of Open Framework Fluoride for Lithium and Sodium Batteries. *Chem. Mater.* **2013**, *25* (6), 962−969.
(31) Li, B.; Rooney, D. W.; Zhang, N.; Sun, K. An In Situ Ionic-Liquid-Assisted Synthetic Approach to Iron Fluoride/Graphene Hybrid Nanostructures as Superior Cathode Materials for Lithium Ion Batteries. *ACS Appl. Mater. Interfaces* **2013**, *5* (11), 5057−5063.
(32) Wei, S.; Wang, X.; Jiang, M.; Zhang, R.; Shen, Y.; Hu, H. The $FeF_3{\cdot}0.33H_2O$/C Nanocomposite with Open Mesoporous Structure as High-Capacity Cathode Material for Lithium/Sodium Ion Batteries. *J. Alloys Compd.* **2016**, *689*, 945−951.
(33) Han, Y.; Hu, J.; Yin, C.; Zhang, Y.; Xie, J.; Yin, D.; Li, C. Iron-Based Fluorides of Tetragonal Tungsten Bronze Structure as Potential Cathodes for Na-Ion Batteries. *J. Mater. Chem. A* **2016**, *4* (19), 7382−7389.
(34) Cao, D.; Yin, C.; Shi, D.; Fu, Z.; Zhang, J.; Li, C. Cubic Perovskite Fluoride as Open Framework Cathode for Na-Ion Batteries. *Adv. Funct. Mater.* **2017**, *27* (28), 1701130.
(35) Liu, M.; Wang, X.; Zhang, R.; Liu, L.; Hu, H.; Wang, Y.; Wei, S. Hollow Porous $FeF_3{\cdot}0.33H_2O$ Microspheres by $AlPO_4$ Coating as a Cathode Material of Na-Ion Batteries. *J. Energy Storage* **2018**, *18*, 103−111.
(36) Rao, R. S.; Pralong, V.; Varadaraju, U. V. Facile Synthesis and Reversible Lithium Insertion Studies on Hydrated Iron Trifluoride $FeF_3{\cdot}0.33H_2O$. *Solid State Sci.* **2016**, *55*, 77−82.
(37) Liu, L.; Zhou, M.; Yi, L.; Guo, H.; Tan, J.; Shu, H.; Yang, X.; Yang, Z.; Wang, X. Excellent Cycle Performance of Co-Doped FeF_3/C Nanocomposite Cathode Material for Lithium-Ion Batteries. *J. Mater. Chem.* **2012**, *22* (34), 17539.
(38) Liu, M.; Wang, X.; Wei, S.; Hu, H.; Zhang, R.; Liu, L. Cr-Doped $Fe_2F_5{\cdot}H_2O$ with Open Framework Structure as a High Performance Cathode Material of Sodium-Ion Batteries. *Electrochim. Acta* **2018**, *269*, 479−489.
(39) Bai, Y.; Zhou, X.; Jia, Z.; Wu, C.; Yang, L.; Chen, M.; Zhao, H.; Wu, F.; Liu, G. Understanding the Combined Effects of Microcrystal Growth and Band Gap Reduction for $Fe_{(1-x)}Ti_xF_3$ Nanocomposites as Cathode Materials for Lithium-Ion Batteries. *Nano Energy* **2015**, *17*, 140−151.
(40) Yang, Z.; Pei, Y.; Wang, X.; Liu, L.; Su, X. First Principles Study on the Structural, Magnetic and Electronic Properties of Co-Doped FeF_3. *Comput. Theor. Chem.* **2012**, *980*, 44−48.
(41) Duttine, M.; Dambournet, D.; Penin, N.; Carlier, D.; Bourgeois, L.; Wattiaux, A.; Chapman, K. W.; Chupas, P. J.; Groult, H.; Durand, E.; Demourgues, A. Tailoring the Composition of a Mixed Anion Iron-Based Fluoride Compound: Evidence for Anionic Vacancy and Electrochemical Performance in Lithium Cells. *Chem. Mater.* **2014**, *26* (14), 4190−4199.
(42) Fan, X.; Hu, E.; Ji, X.; Zhu, Y.; Han, F.; Hwang, S.; Liu, J.; Bak, S.; Ma, Z.; Gao, T.; Liou, S.-C.; Bai, J.; Yang, X.-Q.; Mo, Y.; Xu, K.; Su, D.; Wang, C. High Energy-Density and Reversibility of Iron Fluoride Cathode Enabled via an Intercalation-Extrusion Reaction. *Nat. Commun.* **2018**, *9* (1), 2324.
(43) Yang, J.; Xu, Z.; Zhou, H.; Tang, J.; Sun, H.; Ding, J.; Zhou, X. A Cathode Material Based on the Iron Fluoride with an Ultra-Thin Li_3FeF_6 Protective Layer for High-Capacity Li-Ion Batteries. *J. Power Sources* **2017**, *363*, 244−250.
(44) Jiang, M.; Wang, X.; Wei, S.; Shen, Y.; Hu, H. An Ionic-Liquid-Assisted Approach to Synthesize a Reduced Graphene Oxide Loading Iron-Based Fluoride as a Cathode Material for Sodium-Ion Batteries. *J. Alloys Compd.* **2016**, *670*, 362−368.
(45) Jiang, M.; Wang, X.; Hu, H.; Wei, S.; Fu, Y.; Shen, Y. In Situ Growth and Performance of Spherical $Fe_2F_5{\cdot}H_2O$ Nanoparticles in Multi-Walled Carbon Nanotube Network Matrix as Cathode Material for Sodium Ion Batteries. *J. Power Sources* **2016**, *316*, 170−175.
(46) Liu, J.; Liu, W.; Ji, S.; Wan, Y.; Gu, M.; Yin, H.; Zhou, Y. Iron Fluoride Hollow Porous Microspheres: Facile Solution-Phase Synthesis and Their Application for Li-Ion Battery Cathodes. *Chem. - Eur. J.* **2014**, *20* (19), 5815−5820.
(47) Li, L.; Meng, F.; Jin, S. High-Capacity Lithium-Ion Battery Conversion Cathodes Based on Iron Fluoride Nanowires and Insights into the Conversion Mechanism. *Nano Lett.* **2012**, *12* (11), 6030−6037.
(48) Li, L.; Yu, Y.; Meng, F.; Tan, Y.; Hamers, R. J.; Jin, S. Facile Solution Synthesis of α-$FeF_3{\cdot}3H_2O$ Nanowires and Their Conversion to α-Fe_2O_3 Nanowires for Photoelectrochemical Application. *Nano Lett.* **2012**, *12* (2), 724−731.
(49) Lu, Y.; Wen, Z.; Jin, J.; Rui, K.; Wu, X. Hierarchical Mesoporous Iron-Based Fluoride with Partially Hollow Structure: Facile Preparation and High Performance as Cathode Material for Rechargeable Lithium Ion Batteries. *Phys. Chem. Chem. Phys.* **2014**, *16* (18), 8556.
(50) Trogadas, P.; Ramani, V.; Strasser, P.; Fuller, T. F.; Coppens, M.-O. Hierarchically Structured Nanomaterials for Electrochemical Energy Conversion. *Angew. Chem., Int. Ed.* **2016**, *55* (1), 122−148.
(51) Gao, B.; Li, X.; Ding, K.; Huang, C.; Li, Q.; Chu, P.; Huo, K. Recent Progress of Nanostructured Transition Metal Nitrides for Advanced Electrochemical Energy Storage. *J. Mater. Chem. A* **2018**, DOI: 10.1039/C8TA05760E.
(52) Niu, Z.; Li, Y. Removal and Utilization of Capping Agents in Nanocatalysis. *Chem. Mater.* **2014**, *26* (1), 72−83.
(53) Muraliganth, T.; Vadivel Murugan, A.; Manthiram, A. Facile Synthesis of Carbon-Decorated Single-Crystalline Fe_3O_4 Nanowires and Their Application as High Performance Anode in Lithium Ion Batteries. *Chem. Commun.* **2009**, No. 47, 7360.

DOI: 10.1021/acsaem.8b01585
ACS Appl. Energy Mater. XXXX, XXX, XXX−XXX

(54) Li, Z.; Xiong, Y.; Xie, Y. Selected-Control Synthesis of ZnO Nanowires and Nanorods via a PEG-Assisted Route. *Inorg. Chem.* **2003**, *42* (24), 8105−8109.
(55) Herrmann, S.; Mohl, S.; Siepmann, F.; Siepmann, J.; Winter, G. New Insight into the Role of Polyethylene Glycol Acting as Protein Release Modifier in Lipidic Implants. *Pharm. Res.* **2007**, *24* (8), 1527−1537.
(56) Xu, Y.; Jiao, X.; Chen, D. PEG-Assisted Preparation of Single-Crystalline Cu_2O Hollow Nanocubes. *J. Phys. Chem. C* **2008**, *112* (43), 16769−16773.
(57) Tang, Y.; An, J.; Xing, H.; Wang, X.; Zhai, B.; Zhang, F.; Song, Y.; Li, G. Synthesis of Iron-Fluoride Materials with Controlled Nanostructures and Composition through a Template-Free Solvothermal Route for Lithium Ion Batteries. *New J. Chem.* **2018**, *42* (11), 9091−9097.
(58) Xie, X.-Y.; Li, L.-Y.; Zhan, P.; Liang, M.; Xie, S.-M.; Meng, J.-X.; Bai, Y.; Zheng, W.-J. Fast One-Step Synthesis of ZnO Sub-Microspheres in PEG200. *J. Mater. Sci.* **2014**, *49* (5), 2355−2361.
(59) Hu, Y.; Ding, H.; Li, C. Preparation of Hollow Alumina Nanospheres via Surfactant-Assisted Flame Spray Pyrolysis. *Particuology* **2011**, *9* (5), 528−532.
(60) Burbano, M.; Duttine, M.; Borkiewicz, O.; Wattiaux, A.; Demourgues, A.; Salanne, M.; Groult, H.; Dambournet, D. Anionic Ordering and Thermal Properties of $FeF_3{\cdot}3H_2O$. *Inorg. Chem.* **2015**, *54* (19), 9619−9625.
(61) Feng, Y.; Zhang, M.; Guo, M.; Wang, X. Studies on the PEG-Assisted Hydrothermal Synthesis and Growth Mechanism of ZnO Microrod and Mesoporous Microsphere Arrays on the Substrate. *Cryst. Growth Des.* **2010**, *10* (4), 1500−1507.
(62) Wang, G.; Yi, L.; Yu, R.; Wang, X.; Wang, Y.; Liu, Z.; Wu, B.; Liu, M.; Zhang, X.; Yang, X.; et al. $Li_{1.2}Ni_{0.13}Co_{0.13}Mn_{0.54}O_2$ with Controllable Morphology and Size for High Performance Lithium-Ion Batteries. *ACS Appl. Mater. Interfaces* **2017**, *9* (30), 25358−25368.
(63) Xiong, D.; Li, X.; Bai, Z.; Lu, S. Recent Advances in Layered $Ti_3C_2T_x$MXene for Electrochemical Energy Storage. *Small* **2018**, *14*, 1703419.

DOI: 10.1021/acsaem.8b01585
ACS Appl. Energy Mater. XXXX, XXX, XXX−XXX